Monthly Notices of the ROYAL ASTRONOMICAL SOCIETY

MNRAS **512,** 5085–5099 (2022)
Advance Access publication 2022 March 22

https://doi.org/10.1093/mnras/stac781

Eigenvectors of solar magnetic field in cycles 21–24 and their links to solar activity indices

V. V. Zharkova[1,2★] and S. J. Shepherd[2,3]

[1] *Department of MPEE, University of Northumbria, Newcastle upon Tyne, NE1 8ST, UK*
[2] *ZVS Research Enterprise Ltd., London, EC1V 2NX, UK*
[3] *PRIMAL Research Group, Sorbonne University, Paris 75006, France*

Accepted 2022 March 15. Received 2022 March 15; in original form 2022 January 7

ABSTRACT

Using full disc synoptic maps of solar background magnetic field captured from the Wilcox Solar Observatory for 30 latitudinal bands for cycles 21–24, principal components (PCs) or eigenvectors of magnetic oscillations are obtained. The PCs are shown to come in pairs assigned to magnetic waves produced by dipole, quadruple, sextuple, and octuple magnetic sources. The first pair is linked to dipole magnetic waves with their summary curve revealing a reasonable fit to the averaged sunspot numbers in cycles 21–24. This verifies the previous results and confirms the summary curve as additional proxy of solar activity decreasing towards grand solar minimum in cycles 25–27. There is also a noticeable asymmetry in latitudinal distributions of these PCs showing an increased activity in Northern hemisphere in odd cycles and in Southern hemisphere in even ones similar to the N–S asymmetries observed in sunspots. The second pair of PCs linked to quadruple magnetic sources has 50 per cent smaller amplitudes than the first, while their summary curve correlates closely with soft X-ray fluxes in solar flares. Flare occurrences are also linked to variations of the next two pairs of eigenvectors, quadruple and sextuple components, revealing additional periodicity of about 2.75–3.1 yr similar to observed oscillations in flares. Strong latitudinal asymmetries in quadruple and sextuple components are correlating with the N–S asymmetries of flare occurrences skewed to Southern hemisphere in even cycles and to Northern hemisphere in odd ones. Principal component analysis of solar magnetic field raises perspectives for simultaneous prediction of general and flaring solar activity.

Key words: methods: data analysis – methods: miscellaneous – Sun: activity – Sun: magnetic field – flares – sunspots.

1 INTRODUCTION

Solar activity is currently expressed with the monthly sunspot numbers averaged from many observatories showing regular maxima and minima every 11 yr (Schwabe 1843; Wolf 1850a,b) with the leading magnetic polarity of sunspots changing every 11 yr giving the full cycle for every 22 yr (Hathaway, Wilson & Reichmann 2002; Hathaway 2015). For the future reference in this paper, let us use the averaged sunspot numbers published in the Royal Belgium Observatory (SILSO World Data Center 2021). The prediction of a solar cycle through sunspot numbers has been used for decades as the way of testing the knowledge of mechanisms of the solar dynamo, e.g. processes providing production, transport, and disintegration of the solar magnetic fields.

The solar activity had a modern warming period in cycles 19–21 (Solanki et al. 2004; Usoskin 2008, 2017; Usoskin, Solanki & Moss 2009; Solanki & Krivova 2011) when sunspot numbers were growing with a cycle number before cycle 20. However, the averaged sunspot numbers were becoming lower and lower in cycles 21–24. Now in cycle 25, the solar activity continues to be even lower as can be seen in the steepest increase of spotless days at the start of cycle 25 seen in the past 3 centuries as shown in Fig. 1 taken from the Sunspot Index and Long-term Solar Observations (SILSO) data/image, Royal Observatory of Belgium, Brussels (SILSO World Data Center 2021). The current solar cycle 25 transition counts already more spotless days than the previous one (currently at 848 versus 817 during the SC23–24 transition) that indicates a start of a deeper solar minimum, possibly a grand solar minimum (GSM; Zharkova et al. 2015).

The thick green line in the plot of Fig. 1 shows the accumulated (total number of) spotless days so far during the transit from solar cycle 24 to 25. The thick blue and red lines show the same parameter, but, respectively, for the average of solar cycles 10–15 and 24 (SCo), and of solar cycles 16–23 (SCn). This distinction is made because the first group has a long delay (about 4 yr) and many spotless days (almost 800 on the average), whereas the other group has barely 2 yr between the month with the 10th spotless day and the cycle minimum, and not even half of the total number of spotless days of the first group (less than 400 d!).

Recently, Zharkova, Shepherd & Zharkov (2012) and Zharkova et al. (2015) suggested that instead of the averaged sunspot numbers one can use a new proxy of solar activity derived with principal component analysis (PCA) – the summary curve of two principal components (PCs) of the solar background magnetic field (SBMF) measured from the Wilcox Solar Observatory (WSO) low-resolution synoptic magnetic maps. The maps are produced in the 30 data points in equal steps of sine latitude from +14.5/15 to −14.5/15, and for

★ E-mail: valentina.zharkova@northumbria.ac.uk and Zharkova valja46@gmail.com

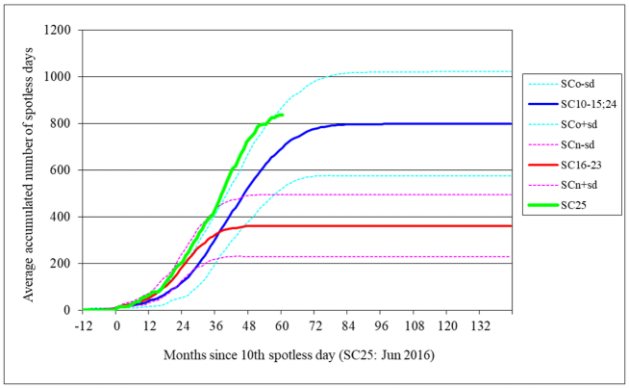

Figure 1. Evolution of spotless days in solar cycles SC24–25 and comparison with the other cycle transits. From the SILSO data/image, Royal Observatory of Belgium, Brussels (https://wwwbis.sidc.be/silso/spotless).

every 5° points of solar longitude range (0–360°). PCA offers a way to extract separate eigenvectors maintained in time reflecting separate physical processes. By averaging the longitudinal data and applying PCA to the magnetic maps in the 30 points of latitude for times of cycles 21–23 (Zharkova et al. 2012), the authors identified the eigenvalues and eigenvectors, or the periodical magnetic waves, generated in the solar interior by various magnetic sources.

Previously, the PCA was conducted by a few authors (Lawrence, Cadavid & Ruzmaikin 2005) using the National Solar Observator (NSO)/ Kitt Peak Solar Observatory (KPNO) data containing the full disc synoptic magnetic maps taken with much higher spatial resolution (1.5 arcsec) than the WSO ones (20 arcsec). The temporal and latitudinal distributions of solar magnetic field were considered for mean B and median B_M magnetic fields averaged in longitudes. In addition, the authors (Cadavid et al. 2005; Lawrence et al. 2005) did further correction of the NSO butterfly diagrams by using the subtracted magnetic data with 6 CR difference proposed by Benevolenskaya (1995) that makes the magnetic data further randomized.

The results by Lawrence et al. (2005) for the mean field B were close in some aspects to those derived by Zharkova et al. (2012) having the two PCs, which follow 22 yr periodicity of solar cycle, like sunspots. The further investigation of the NSO data was carried out using an independent component analysis (ICA) applied to this difference magnetic data in an attempt to find further fundamental oscillation modes free of noise (Cadavid et al. 2005). This approach helped us to identify the additional periods of magnetic field oscillations occurring in the solar interior slightly varying from the solar pole to equator (1.3–1.7 yr; Cadavid et al. 2005), besides a 22 yr cycle derived with PCA (Lawrence et al. 2005; Zharkova et al. 2012).

However, the findings by Lawrence et al. (2005), Cadavid et al. (2005), and Cadavid, Lawrence & Ruzmaikin (2008) did not reveal clear pairs of the components and did not find their links to the observable indices of solar activity, like those found by Zharkova et al. (2012). The absence of paired components can be understood in terms of a much higher spatial resolution of the NSO full disc magnetic data, which includes not only the solar background (poloidal) magnetic field but also the (toroidal) magnetic fields of active regions clearly shown in the magnetic 'butterfly diagrams' (Lawrence et al. 2005).

This means that the NSO data entered into the PCA or ICA by Lawrence et al. (2005), Cadavid et al. (2005), and Cadavid et al. (2008) were strongly contaminated by the magnetic field of active regions and sunspots (reaching up to 1000 G). However, the WSO low-resolution magnetic data have these active region magnetic fields significantly smoothed to match the background field; e.g. a magnetic loop with a magnetic field 1000 G (from NSO with a pixel area approximately $1''.5 \times 1''.5 = 2''.25$, or for simplicity 2 arcsec × 2 arcsec = 4) can be observed in the WSO (pixel area 20 arcsec × 20 arcsec = 400) as 1000 Gx 4/400 = 10 G, or even 5 G for $1''.5$ resolution. Hence, each pixel in the WSO magnetic maps becomes a background magnetic field unlike the NSO containing magnetic fields of active regions.

As a result, their PCA produces rather smooth distributions of eigenvalues in their Spree plots (Cadavid et al. 2005; Lawrence et al. 2005) and does not show clear separation of the eigenvectors into pairs detected in the PCA by Zharkova et al. (2012). These differences restricted the PCA for the NSO data to detecting the background (poloidal) magnetic field near solar poles and the magnetic (toroidal) fields of active region in the royal zone ±35° about the solar equator (Cadavid et al. 2005; Lawrence et al. 2005). However, the PCA of the WSO magnetic data can be attributed to the SBMF in the whole solar disc as suggested (Zharkova et al. 2012, 2015).

Each set of the PCs detected from the NSO and WSO magnetic data has its own value for the dynamo modelling, while both the data are rather close at higher latitudes, emphasizing the role of SBMF via polar magnetic field (Benevolenskaya 1996, 1998; Cadavid et al. 2005; Choudhuri, Chatterjee & Jiang 2007). The first pair, or two PCs detected by Zharkova et al. (2012) resembling the two first PCs derived from the NSO data (Cadavid et al. 2005; Lawrence et al. 2005), was shown to reflect the primary waves of solar magnetic dynamo with a period of 22 yr produced by the dipole magnetic sources (Benevolenskaya 1998; Zharkova et al. 2015). The link of the summary curve of these PCs with the solar activity index of the average sunspot numbers reported by Shepherd, Zharkov & Zharkova (2014) and Zharkova et al. (2015) can be clearly understood because these PCs, in fact, reflect the magnetic butterfly diagrams linked to sunspot occurrences (Cadavid et al. 2005; Lawrence et al. 2005).

The two magnetic waves are found travelling slightly off-phase while moving from one hemisphere to another (Zharkova et al. 2012). Then, Shepherd et al. (2014) and Zharkova et al. (2015) used the symbolic regression analysis (Schmidt & Lipson 2009) of these two magnetic waves and obtained the analytical expressions describing the magnetic waves incorporated into the SBMF derived for cycles 21–23 (Zharkova et al. 2012) and attributed to the poloidal field of the solar dynamo (Popova, Zharkova & Zharkov 2013). These mathematical equations were used to make predictions of the two PCs in time, both forward and backward, by a few thousand years and to use them for a comparison with the two-layer solar dynamo model with meridional circulation (Zharkova et al. 2015).

The temporal features of the summary curve of these two PCs, namely its modulus curve used to exclude magnetic polarity, have shown a remarkable resemblance of this curve to the sunspot index of solar activity for cycles 21–23 (Zharkova et al. 2015), despite the fact that the summary curve of these PCs reflects the solar poloidal magnetic field while the sunspot index is associated with a toroidal magnetic field of the Sun. This similarity allowed the authors to suggest this summary curve of SBMF as a new solar activity proxy. The advantage of using the summary curve instead of the averaged sunspot numbers is a presence of the extra parameter, a leading polarity of SBMF, which is shown to be in the antiphase with the magnetic polarity of leading sunspots (Zharkov, Gavryuseva & Zharkova 2008).

Using the derived formulae, the summary curve was calculated backwards for 800–1200 yr, revealing the very distinct variations

of cycle amplitudes in every 350–400 yr or grand solar cycles. These grand cycles are separated by GSMs, when the amplitudes of 11 yr cycles become very small, similar to those reported in Maunder, Wolf, and Oort GSMs. The timings of GSMs are defined by the interference of two magnetic dynamo waves with close but not equal frequencies (so-called beating effect) defined by the different velocities of meridional circulation (Zharkova et al. 2015). The calculation of the summary curve forwards in time until 3200 has also shown the further three grand solar cycles separated by three GSMs with the first GSM to occur in the cycles 25–27, or in 2020–2053 (Zharkova et al. 2015; Zharkova 2020). The various aspects of the criticism (Usoskin & Kovaltsov 2015; Usoskin 2018) of the data used (Zharkova et al. 2015) the derived formulae for two PCs of SBMF, the use of the summary curve of these PCs as a new proxy for the prediction of long-term solar activity, and exploring the role of dipole and quadruple components (QCs; Popova et al. 2018) was clearly answered and the results verified in a few papers (Zharkova et al. 2017, 2018).

There were some objections (Svalgaard & Schatten 2016) to prediction of the upcoming GSM in the next 32 yr (Zharkova et al. 2015) and the existence of GSMs in the past, similar to the recorded Oort, Wolf, and Maunder grand minima. However, more recent papers verified the GSM existence in the past (Chatzistergos et al. 2017) and confirmed the prediction of the modern GSM in cycles 25–27 (Kitiashvili 2020; Obridko et al. 2021) by comparing the spectra of zonal harmonics of the SBMF and three-dimensional solar dynamo models using the same WSO synoptic magnetic field data as Zharkova et al. (2015). Furthermore, Velasco Herrera, Soon & Legates (2021) applied the machine learning algorithm to the averaged sunspot numbers taken from the International Sunspot Number (SSN) from the World Data Center SILSO (SILSO World Data Center 2021) and obtained similar results reporting the modern GSM to occur in cycles 25–27, similarly to that reported by Zharkova et al. (2015).

The advantage of using PCA is to separate the eigenvectors defining different physical processes. So far, we managed to establish a correspondence of the summary curve of SBMF, produced by the dipole magnetic field, to the production of sunspot numbers defining solar cycles of 11 yr (Shepherd et al. 2014; Zharkova et al. 2015). However, the properties of these links are not fully explored yet. There were studies of the periodicity in the N–S asymmetry of sunspot areas from cycles in 1874–1989 (Carbonell, Oliver & Ballester 1993; Ravindra, Chowdhury & Javaraiah 2021) and 1874–1993 (Oliver & Ballester 1994) and 1974–2020 (Leussu et al. 2016; Veronig et al. 2021). The authors reported a well-defined north–south asymmetry in all solar cycles and demonstrated with the Monte Carlo modelling (Oliver & Ballester 1994) that the N–S asymmetry cannot be generated by stochastic processes. The similar N–S asymmetry in sunspot numbers was reported for cycles 20, 21, and 22 (Temmer, Veronig & Hanslmeier 2002) and cycle 23 (Zharkov, Zharkova & Ipson 2005). Also, there was the N–S asymmetry discovered in the sunspot magnetic fields in cycle 23 derived from the Michelson Doppler Imager (MDI) white light and magnetogram full disc images with the automated detection techniques (Zharkov et al. 2005; Zharkov & Zharkova 2006).

In addition, a good correlation is established between the soft X-ray (SXR) fluxes in flares and the occurrences of H α flares (Vizoso & Ballester 1989; Özgüç, Ataç & Rybák 2003; Zharkov & Zharkova 2011) showing short-term oscillations with significant peaks in the power spectrum of H α flare occurrences around 3.1–3.2 yr in cycle 22 (Vizoso & Ballester 1989) or around 2.75 yr in cycle 23 (Zharkov & Zharkova 2011).

Some authors have made extensive statistical analysis of H α flares, finding its good correlation with a number of solar indices that arise under different physical conditions (Atac 1989; Ataç & Özgüç 1996; Özgüç et al. 2003). There were also distinct peaks at 26.5 and 28.3 d reported in the power spectrum of solar radio flux at 10.7 cm for the Northern and Southern hemispheres (Joshi 1999) and for a few other solar indices (Atac 1989; Pap, Willson & Donnelly 1992; Ataç & Özgüç 1996; Özgüç et al. 2003; Temmer 2021). Zharkov & Zharkova (2011) established a strong link of H α flare occurrences and averaged sunspot numbers and their magnetic field revealing also a clear N–S asymmetry in the H α flare occurrences, e.g. in cycle 22 Özgüç & Altaş (1996) and 23 (Zharkov & Zharkova 2011). The N–S asymmetry was also reported in the SXR flare fluxes in cycles 21–23, which is based on the continuous record of SXR flares observed by Geostationary Operational Environmental Satellite (GOES, Joshi & Joshi 2004; Joshi et al. 2010, 2015).

The N–S asymmetry observed in the SXR fluxes of solar flares in cycles 21–23 was proven to not occur due to random fluctuations (Joshi & Joshi 2004; Joshi et al. 2010, 2015). It was shown that during the solar cycle 21, the Northern hemisphere was more active in the production of SXR flux of solar flares but after 1980 it was shifted slightly towards south. In the year 1983, the activity moved towards south strongly and prevailed there during most of the solar cycle 22. In the solar cycle 23, we observe a strong peak in Southern hemisphere during the minimum phase in the year 1996 and then the activity is moved towards the north. In the years 1998, 1999, and 2000, the Northern hemisphere was dominated. These results are in agreement with the N–S asymmetry of H α flares detected from 1975 to 1999 (Temmer et al. 2001) or from 1996 until 2005 (Zharkov & Zharkova 2011). The preference for Northern hemisphere in the data of H α flares during the rising phase of cycle 23 is also reported by Ataç & Özgüç (2001), who also noticed that the behaviour of asymmetry is changed in 2000 and it shifted towards Southern hemisphere in the successive years.

So far, there were no viable ideas proposed for the explanation of this N–S asymmetry that can be resolved with help of the eigenvectors of solar oscillations derived with PCA. The solar magnetic field oscillations derived with PCA give some positive breakthrough in this problem having detected not only magnetic waves produced by dipole magnetic sources of the Sun's poles but also other magnetic waves produced by quadruple, sextuple, or octuple magnetic sources. These additional magnetic waves can be responsible for the shifts of active feature occurrences in the Northern hemisphere with respect to the southern one imposed by the appearance of the additional magnetic sources that could be affected by different differential rotation velocities in the opposite hemispheres. For example, Antonucci, Hoeksema & Scherrer (1990) first reported in cycle 21 a dominant period of 26.9 d for the Northern hemisphere and 28.1 d for the Southern hemisphere. The similar outcome was confirmed later from the power spectral analysis of daily sunspot numbers during 1975–2000, deriving a rigid rotation with 27.0 d for the Northern hemisphere and 28.2 d for the Southern hemisphere (Temmer et al. 2002). These shifts in the differential rotations of Northern and Southern hemispheres can lead to a redistribution of magnetic sources and formation of quadruple, sextuple, and other magnetic sources.

Hence, in order to improve the accuracy of the new solar activity proxy (summary curve) and prediction of solar activity on a millennium time-scale (Zharkova et al. 2015), it would be useful to extend PCA to the new data of cycle 24 and to add for consideration of the next PCs of the magnetic waves of the Sun derived from the SBMF, e.g. the next four or six eigenvectors defined by lower variances. The first attempt of such an addition was done by adding theoretical

curve for magnetic waves produced by solar dynamo for quadruple magnetic sources (Popova et al. 2018). More beneficial would be to investigate the next pairs of eigenvectors derived from the SBMF with PCA and to explore how their addition is linked to the observations of solar activity feature (sunspots, active regions, solar flares, etc.). The resulting magnetic wave obtained from the joint effect of the dipole and quadruple waves can change the visible appearance of solar activity curves and produce some additional features, possibly, not accounted for before.

The new eigenvalues and vectors derived from the SBMF synoptic maps for cycles 21–24 are described in Section 2, the comparison of the summary curves of the first and second pairs and their links with solar activity features are discussed in Section 3, and the discussion and conclusions are drawn in Section 4.

2 PCA OF THE SOLAR BACKGROUND MAGNETIC FIELD

2.1 Derived eigenvectors in cycles 21–24

2.1.1 Brief description of PCA methodology

In order to derive the main periods present in the observational data of SBMF at different latitudes, let us apply PCA to the whole set of two-dimensional (2D) magnetic field data for cycles 21–24 varying in time and latitude to derive the eigenvalues and dominant eigenvectors and to compare them with those components derived earlier for cycles 21–23 (Zharkova et al. 2012).

PCA is an orthogonal linear transformation allowing a vector space to be transformed to a new coordinate system, reducing the multidimensional data Y to lower dimensions for better analysis, so that the greatest variance by any projection of the data lies on the first coordinate called the PC (Jolliffe 2002). The inner (respectively, outer) PCs of a data set represented by an $(m \times n)$ matrix X, or so-called PCs, are computed by projecting the original data X into the eigenspace of the data covariance matrices (Jolliffe 2002).

The standard context for PCA as an exploratory data analysis tool involves a data set with observations on m numerical variables, for each of the n entities or individuals. These data values define $(m \times n)$-dimensional vectors $Y_1,..., Y_m$ or, equivalently, an $(n \times m)$ data matrix Y, whose j-th column is the vector y_j of observations on the j-th variable. We seek a linear combination of the columns of matrix **Y** with a maximum variance.

Such linear combinations are given by the vector $\mathbf{X} = \Sigma_{j=1}^{m} a_j y_j = \mathbf{Ya}$, where **a** is a vector of constants $a_1, a_2,..., a_m$. The variance of such a linear combination is given by $\mathrm{var}(\mathbf{Ya}) = \mathbf{a^T S a}$, where **S** is the sample covariance matrix associated with the data set and the sign 'T' denotes 'transposed'.

Hence, identifying the linear combination with maximum variance is equivalent to obtaining an m-dimensional vector **a**, which maximizes the quadratic form $\mathbf{a^T S a}$. For this problem to have a well-defined solution, an additional restriction must be imposed and the most common restriction involves working with unit-norm vectors, i.e. requiring $\mathbf{a^T a} = 1$.

The problem is equivalent to maximizing $\mathbf{a^T S a} - \lambda(\mathbf{a^T a} - 1)$, where λ is a Lagrange multiplier. This resu lts in the equation defining the eigenvalues λ as follows:

$$\mathbf{Sa} - \lambda\mathbf{a} = 0. \tag{1}$$

Thus, **a** must be a (unit-norm) eigenvector, and λ the corresponding eigenvalue, of the covariance matrix **S**. In particular, we are interested in the largest eigenvalue, λ_1 (and corresponding eigenvector $\mathbf{a}_1$), since the eigenvalues are the variances of the linear combinations defined by the corresponding eigenvector **a**:

$$\mathrm{var}(\mathbf{Ya}) = \mathbf{a^T S a} = \lambda\mathbf{a^T a} = \lambda. \tag{2}$$

Hence, the signs of all loadings (and scores) are arbitrary and only their relative magnitudes and sign patterns are meaningful. Any $(m \times m)$ real symmetric matrix, such as a covariance matrix **S**, has exactly m real eigenvalues, λ_k $(k = 1,..., m)$, and their corresponding eigenvectors can be defined to form an orthonormal set of vectors. These linear combinations $\vec{X} = \mathbf{Ya_k}$ are called the PCs of the data set.

The PCs *(of the data set variations in time)* are those vectors of X that are associated with the largest eigenvalues λ. In practice, we sort the diagonal of λ (the eigenvalues of **a**) in a descending order of the magnitude together with the corresponding rows (or columns for the outer PC) of **a** (the eigenvectors $\mathbf{a_k}$ of **a**).

PCs are new variables that are constructed as linear combinations or mixtures of the initial variables. These combinations are done in such a way that the new variables (i.e. PCs) are uncorrelated and most of the information within the initial variables is squeezed or compressed into the first components. Geometrically speaking, PCs represent the directions of the data that explain a maximal amount of variance, which is to say, the lines that capture most information of the data. The relationship between variance and information here is that the larger the variance carried by a line, the larger the dispersion of the data points along it, and the larger the dispersion along a line, the more information it has.

For most data sets arising from naturally observed phenomena where the data are noisy, there are comparatively few dominant eigenvalues, which represent the real signal in the data. Thus, this technique simultaneously (i) reduces the data dimensionality, (ii) separates the signals from noise, and (iii) orthogonalizes the resulting components so that they can be ascribed to separate physical processes.

2.2 Singular value decomposition (SVD) of 2D eigenvectors

In linear algebra, the SVD is a factorization of a real or complex matrix (Golub & Kahhan 1965; Golub & Van Loan 1996). It generalizes the eigendecomposition of a square normal matrix with an orthonormal eigenbasis to any $(m \times n)$ matrix.

Specifically, the SVD of an $(m \times n)$ complex matrix **M** is a factorization of the form $\mathbf{U\Sigma V}^*$, where **U** is an $(m \times m)$ complex unitary matrix, Σ is an $(m \times n)$ rectangular diagonal matrix with non-negative real numbers on the diagonal, and **V** is an $(n \times n)$ complex unitary matrix. If **M** is real, **U** and **V** can also be guaranteed to be real orthogonal matrices. In such a context, the SVD is often denoted as $\mathbf{U\Sigma V^T}$, where index 'T' means 'transposed'.

The diagonal entries $\sigma_i = \Sigma_{ii}$ of Σ are known as the singular values of **M**. The number of non-zero singular values is equal to the rank of **M**. The columns of **U** and the columns of **V** are called, respectively, the left-singular vectors and right-singular vectors of matrix **M**.

We use SVD to separate the 2D matrix $\mathbf{X} = \mathbf{M}$ of solar magnetic data obtained after we applied PCA for the 2D magnetic synoptic maps: in latitudes and in time. The eigenvalues λ_i derived from these data with PCA are those σ_i used in SVD. In order to separate the temporal eigenvectors and latitudinal eigenvectors, we apply SVD with the given eigenvalues and obtain the left-singular vectors (dimension of 585) to be temporal ones and the right-singular vectors (dimension of 72) to be latitudinal ones.

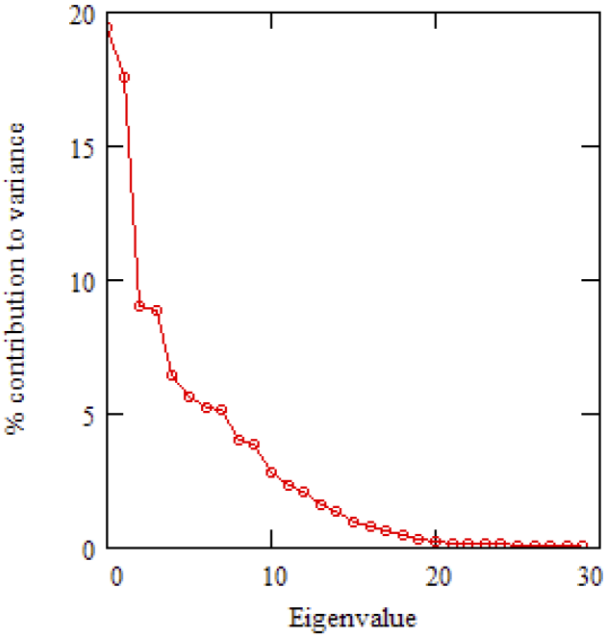

Figure 2. Scree plot: the variance contributions (*Y*-axis) versus the eigenvalue numbers (*X*-axis) derived with the PCA decomposition of the SBMF for solar cycles 21–24 measured from magnetic synoptic maps by the WSO, US (Hoeksema 1984). Note that the Scree plot for the data of four cycles 21–24 is identical to that derived previously for three cycles 21–23 (Zharkova et al. 2012).

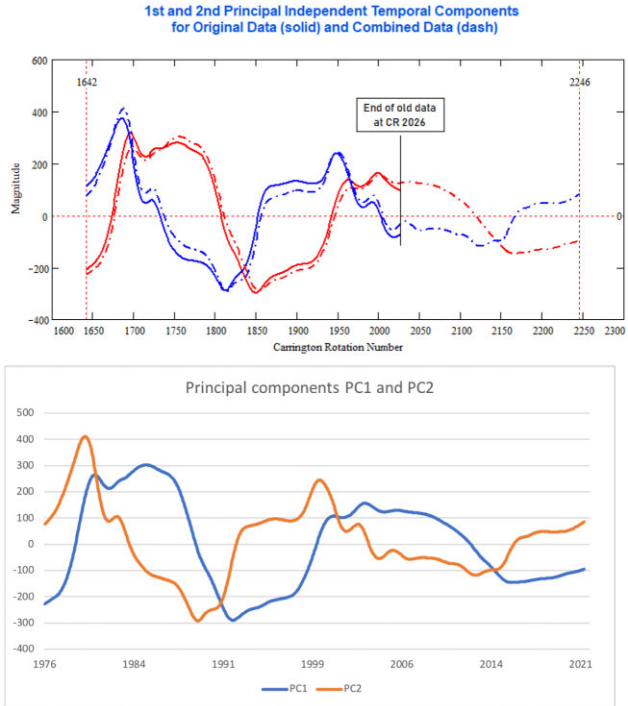

Figure 3. Top: Comparison of the two principal components PC1 and PC2 (*Y*-axis, arbitrary units) derived from the WSO magnetic synoptic maps versus time (*X*-axis) for the cycles 21–24 (dashed line, the current paper) with those derived previously for cycles 21–23 (solid line) (Zharkova et al. 2012). Bottom: The two principal components PC1 and PC2 (*Y*-axis, arbitrary units) derived from the WSO magnetic synoptic maps versus time (*X*-axis) for the cycles 21–24.

2.3 Eigenvectors of SBMF in cycles 21–24

2.3.1 Two temporal principal components – dipole magnetic sources

In the previous studies (Zharkova et al. 2012, 2015), we utilized the WSO 2D synoptic magnetic field data for 30 bands in latitude for a range $\pm 75^\circ$ and in time for cycles 21–23 (Hoeksema 1984), e.g. for Carrington rotations from 1642 to 2026. In the current paper, we added the further 2D synoptic magnetic field data for cycle 24, e.g. up to the CR 2246. By running PCA, the updated set of the eigenvalues of solar magnetic field expressed in the variance assigned to a given component (see Section 2.1.1) is obtained as shown in the Scree plot in Fig. 2. The eigenvalues are found equal to those derived previously from the magnetic field of cycles 21–23 (Zharkova et al. 2012) and they still appear in pairs.

The first pair of the eigenvectors, or two PCs of the waves, corresponding to the first pair of eigenvalues, which has the highest percentage of the data coverage by variance (19 and 20 per cent, respectively) covering about 62.4 per cent of the magnetic field data by a standard deviation (Zharkova et al. 2012). This pair of PCs was assigned to those produced by the solar dynamo in two layers of solar interior by dipole magnetic sources (Zharkova et al. 2015). The sum of two PCs is called a summary curve, which was shown to define a new solar activity index linked also to the averaged sunspot index (Zharkova et al. 2015).

The next pair of QCs covers much less data, 8.6 per cent and 8 per cent, or 16.6 per cent, in total, by variance, respectively, adding extra 11.3 per cent, achieving 74.6 per cent, in total, by a standard deviation. The QCs are assumed to be produced by quadruple magnetic sources (Zharkova et al. 2015; Popova et al. 2018). There are further two pairs of eigenvalues derived in the Scree plot in Fig. 2, which cover the total variance of 13 per cent for the third pair of sextuple components, SCs, and 10 per cent for the fourth pair of octuple components, OCs. They are covering, respectively, 8.2 and 6.2 per cent of data by standard deviation achieving, consequently, 82.8 and 88.7 per cent, in total, if all three or four pairs are considered.

The eigenvalues derived for cycles 21–24 and their relevant eigenvectors are found to be technically undistinguishable from those obtained previously for the synoptic magnetic maps in cycles 21–23 (Zharkova et al. 2012). The two PCs newly derived here for cycles 21–24 are compared with those used earlier for cycles 21–23 (Zharkova et al. 2012) with the result of this comparison plotted in Fig. 3 versus CR numbers (top plot) and calendar years (bottom plot). The new PCs are only slightly shifted along the *Y*-axis for a demonstration of their similarity. It can be clearly seen that both the PC curves for cycles 21–24 and 21–23 have a very close fit, following the same directions and functionalities. This confirms the previous results based on the magnetic field data for cycles 21–23 (Shepherd et al. 2014; Zharkova et al. 2015) and proves that the eigenvalues and eigenvectors of solar magnetic field are the intrinsic properties of the waves produced by solar dynamo, which do not change at all or, at least, do not change very quickly within four cycles.

The two PCs for dipole magnetic waves derived from the extended data for cycles 21–24 are shown in Fig. 3, bottom plot, revealing the extension of both components into cycle 24. Both the PCs (blue and red curves) derived from the historical data in cycles 21–24 show a few clear trends (Zharkova et al. 2012): (i) at the beginning of cycle 21, the oscillations marked by the red curve start in the Northern hemisphere, while those marked by blue start in the Southern one; (ii) both waves approach their maxima either in the Northern hemisphere

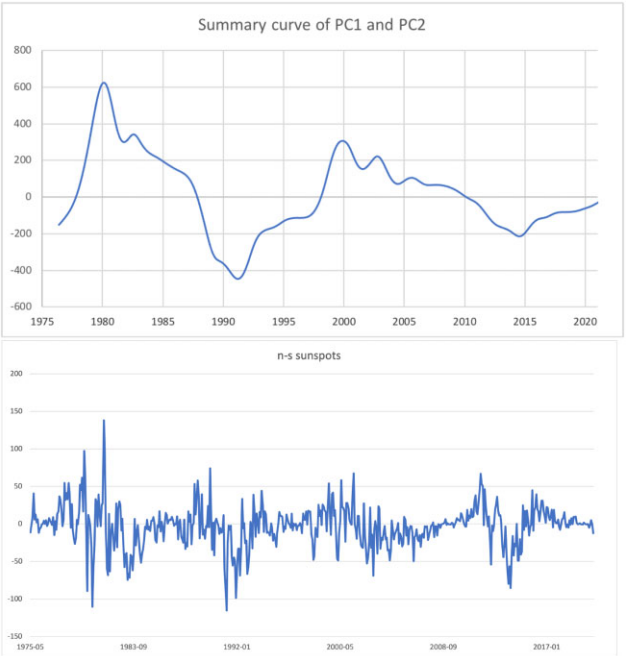

Figure 4. The summary curve of the two principal components PC1 and PC2 from Fig. 3 (*Y*-axis, arbitrary units) versus time (*X*-axis) for the cycles 21–24 (top plot) and the north–south asymmetry of sunspot numbers (SILSO World Data Center 2021) (*Y*-axis) versus time (*X*-axis) for the cycles 21–24 (bottom plot).

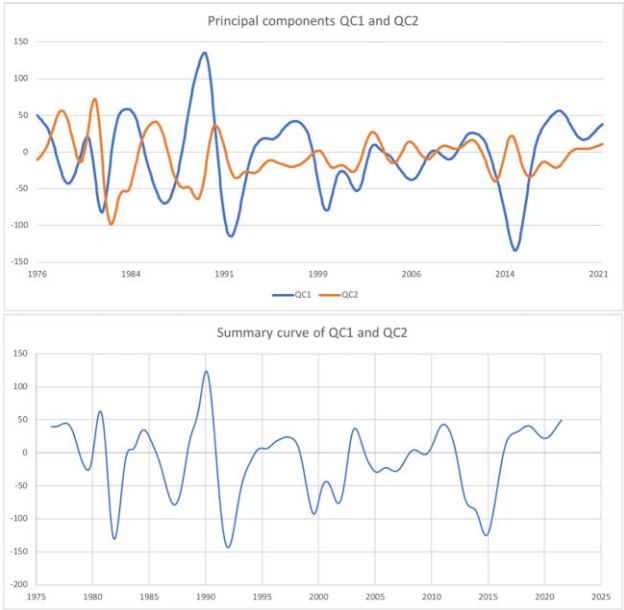

Figure 5. The two quadruple PCs (*Y*-axis, arbitrary units), QCs, of the SBMF data (blue and red lines) (top plot) and their summary curve (bottom plot) plotted versus time (*X*-axis) in cycles 21–24.

(for odd cycles 21 and 23) or in the Southern one (for even cycles 22 and 24); (iii) the maxima of both waves are overlapping either in the Northern hemisphere (for odd cycles 21 and 23) or in the Southern hemisphere (for even cycles 22 and 24), making these hemispheres in a given cycle more active than the opposite one; (iv) the magnitudes of maxima of both the curves are steadily decreasing by approximately 30–40 per cent each cycle from cycle 21 to cycle 24; and (v) a phase difference between the components PC1 and PC2 is increasing with a cycle number.

Curiously enough, the variations of the summary curve shown in Fig. 4, bottom plot, mimic reasonably close the north–south asymmetry in the average sunspot numbers (SILSO World Data Center 2021), confirming the domination of one (PC1) or another (PC2) magnetic wave at a given phase of the cycle seen in Fig. 3, bottom plot. This N–S asymmetry in sunspot numbers was reported from observations for cycles 20, 21, and 22 (Temmer et al. 2002) and cycle 23 (Zharkov et al. 2005). Also, the similar N–S asymmetry was discovered in the sunspot magnetic fields in cycle 23 derived from the full disc MDI white light images and magnetograms (Zharkov et al. 2005; Zharkov & Zharkova 2006). Now these N–S asymmetries can be understood much more clearly, in terms of the reported variations of two eigenvectors of the SBMF shown in Fig. 3 showing the dominant hemisphere where the eigenvectors approach their maxima and, thus, reveal strongest interference.

In order to bring the detected trends in the SBMF closer to the currently used index of solar activity, the averaged sunspot numbers, we calculated the summary component of the two PCs (the top plot in Fig. 4) showing a clear decay of the summary component from cycles 21 to 24 because their amplitudes are reduced. The decay of the summary magnetic wave, representing a poloidal solar magnetic field, is shown to be intrinsic to the mechanism of solar dynamo responsible for generating the two main waves in two different layers of the solar interior (Zharkova et al. 2015). This decay indicates a decrease of the SBMF from cycles 21 to 24 that was already spotted in observations of the solar magnetic field (Lockwood et al. 2011; Solanki & Krivova 2011) and confirmed with a current decrease of the interplanetary magnetic field for the cycle 24 (McComas et al. 2018).

2.3.2 *Two temporal PCs – quadruple magnetic sources*

The next pair of the two eigenvectors, or quadruple (principal) components (QCs), derived with PCA from the SBMF is shown in Fig. 5 (top plot). The QC curves are defined by the two eigenvalues of 8.6 and 8 per cent of the total variance as per the Scree plot (Fig. 2) of the whole solar magnetic field data. By adding these two quadruple (QC) waves to the first two PCs associated with dipole waves, one can improve the accuracy of the data coverage by eigenvectors up to 74.6 per cent by standard deviation. It is evident that the QC amplitudes (Fig. 5, top plot) are nearly twice smaller that that of the first pair of PCs shown in Fig. 4 (top plot). One of the QCs is close to the PC3 shown in fig. 7 in Lawrence et al. (2005).

Furthermore, the temporal variations of QCs are essentially different from those of PCs discussed in Section 2.3.1. First, there is no single maximum per cycle like it was for the PCs but shown a few maxima in each hemisphere. The blue component seems to have larger amplitudes and more maxima with higher magnitudes in the Southern hemisphere (see Fig. 5, top plot). The strongest maximum of northern polarity occurred between 1986 and 1989, while the two strongest maxima of southern polarity occurred between 1990 and 1993 and 2012–2017. This indicates that the QC waves are more pronounced in the Southern hemisphere and this property should be detected in the investigation of the north–south distributions of some solar activity indices different from sunspot numbers.

The summary curve of these two QCs calculated by adding the amplitudes of the components QC1 and QC2 is plotted in Fig. 5 (bottom plot). As result, the summary curve shown in Fig. 5 (bottom plot) shows more maxima into the negative (southern polarity), which

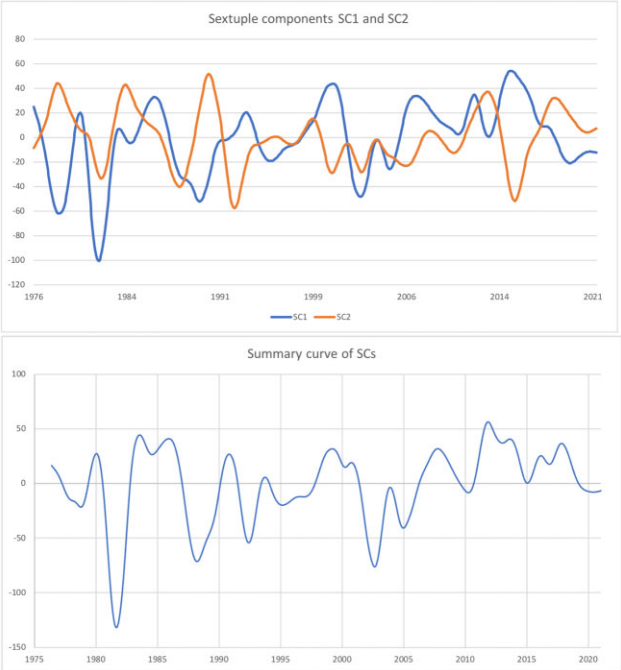

Figure 6. Top plot: the two sextuple PCs (*Y*-axis, arbitrary units), SCs, of the SBMF data (top plot, blue and red lines) and their summary curve (*Y*-axis) (bottom plot) versus time (*X*-axis) obtained for cycles 21–24.

have higher amplitudes, even for the recent solar cycle 24, which had much weaker PCs (see Fig. 4). It reveals that the QC waves produced by quadruple magnetic sources are somehow skewed towards the Southern hemisphere in cycles 21 and 23 having more extrema with larger amplitudes in the Southern hemisphere in comparison with a few occurring in the northern one. The link of this QC with the solar flare features will be discussed in Section 3.2.

2.3.3 *Two temporal PCs from sextuple and octuple sources*

Let us now present the next two pairs of eigenvectors, namely SCs and OCs shown by the two pairs of dots below the two dots defining QCs in the Scree plot in Fig. 2. The two SCs for cycles 21–24 are presented in Fig. 6, while the OCs are presented in Fig. 7.

The two PCs for sextuple magnetic sources, SCs, calculated for cycles 21–24 are presented in Fig. 6, top plot and their summary curve is plotted in Fig. 6, bottom plot. It can be observed that the amplitudes of SCs shown in Fig. 6, top plot are about 20–30 per cent lower that those of the quadruple waves QCs plotted in Fig. 5 because the SC eigenvalues are also slightly lower than the QC ones. The number of extrema (maxima and minima) in the SCs is essentially different from that of the quadruple waves QCs, and they appear at different times. What becomes evident that the two SC components and their summary curve reveal in cycles 23-24 well defined maxima in positive magnitudes (corresponding to northern polarity while in cycle 21 these maxima occurred for negative magnitudes (or southen magnetic polarity). This is different from the quadruple summary curve skewed mainly towards the negative magnitudes (southern polarity) for all cycles.

The next two PC OCs, assigned to octuple magnetic field sources, calculated from the WSO data for cycles 21–24 are presented in Fig. 7. The amplitudes of OCs are further reduced by about 50 per cent compared to the sextuple SCs revealing a large

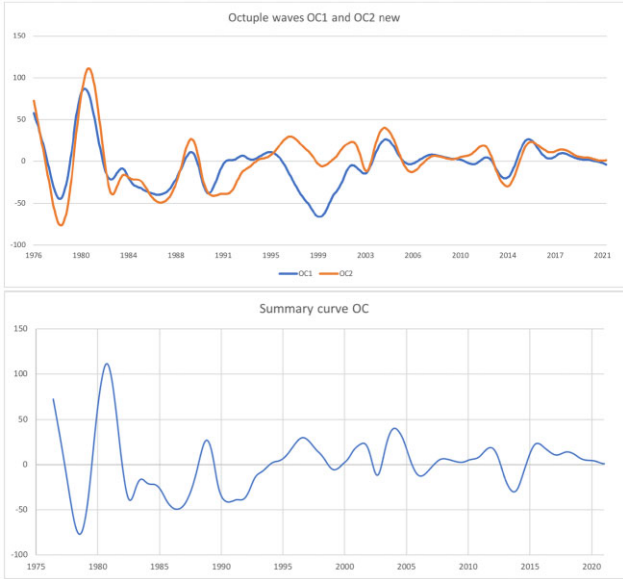

Figure 7. Top plot: the two octuple PC OCs (*Y*-axis, arbitrary units, blue and red lines) of the SBMF data versus time (*X*-axis) for cycles 21–24. Bottom plot: the summary curve (*Y*-axis) of the OCs above (in arbitrary units) versus time for cycles 21–24.

oscillation in cycle 21 and reduction of these oscillation amplitudes with a cycle number. The oscillations of this OC summary are evenly distributed between positive and negative amplitudes or northern and southern polarities.

2.3.4 *Latitudinal components*

Now let us explore the four pairs of the latitudinal principal components (LPCs), or eigenvectors, obtained with SCD approach, which are demonstrated in Fig. 8, which are slightly different in the middle to low latitudes from those shown in fig. 9 by Lawrence et al. (2005) since the current WSO latitudinal distributions are not contaminated by the magnetic fields of active regions present in the NSO data (see the 'Introduction' section). These LPCs are corresponding to the temporal PCs as follows: to two dipole components, PCs (top left plot), two QCs (top right plot), two SCs (bottom left plot), and two OCs (bottom right plot).

It can be noted that the two main latitudinal PCs are rather symmetric functions showing the ways how the temporal PCs travel through each hemisphere if the waves are generated by dipole magnetic sources since the pole polarities are to be changed every solar cycle. The dipole LPCs are in the antiphase in the poles; e.g. they have the opposite magnetic polarities at each pole. The blue curve in latitudinal PC in Fig. 8 (top left plot) (corresponding to the temporal red curve in Fig. 4) starts from the Northern hemisphere, while the red curve in latitude (corresponding to the blue temporal curve in Fig. 4) starts from the southern one.

At higher latitudes beyond $\pm 40^\circ$, the positive wave is in the full antiphase with the negative one, but at lower latitudes both the waves become rather coherent without any phase shift until they reach the latitudes of $\pm 40^\circ$ for the given hemisphere, respectively. In order to achieve this, the positive (negative) magnetic field component passes at about $\pm 40^\circ$ through a wide maximum (minimum) in the Northern hemisphere and a wide minimum (maximum) in the Southern hemisphere, respectively. Then, both waves have their local minimum in the Southern hemisphere about -14° for the negative

Figure 8. The eight latitudinal PCs (*Y*-axis, arbitrary units) versus latitudes (*X*-axis) extracted with SVD from the 2D eigenvectors of the SBMF obtained with PCA from the WSO magnetic synoptic maps for cycles 21–24.

(blue) wave and -18° for the positive (red) one. The latitudes of the positive maxima in the Southern hemisphere and the negative minimum in the northern one are close to the latitudes to which the mean sunspot locations found from the butterfly diagram approach at the end of solar cycle 23 (Zharkova et al. 2012).

In addition, there are other six latitudinal PCs shown in Fig. 8 corresponding to the lower eigenvalues corresponding to the temporal PCs discussed in Sections 2.3.2 and 2.3.3. The next pair of latitudinal wave QCs, supposedly, produced by quadruple magnetic sources (the top right plot in Fig. 8) can help us to understand the propagation of the temporal quadruple wave QCs over the hemispheres. Both (red and blue) the QC waves have zero amplitudes near the poles. The blue (negative) wave has the maxima at 45° and -40° latitudes and minimum at the equator, while the red (positive) wave has a maximum about the equator, a minimum at -30° and another maximum at -55° of the southern latitude. These plots clearly indicate that the quadruple latitudinal wave QCs are noticeably skewed towards the Southern hemisphere, where both the wave maxima are well defined and higher than those in the northern one.

The opposite happens with the next pair of the latitudinal PCs – sextuple wave SCs (Fig. 8, bottom left plot). Both (blue and red) the waves pass through a few extrema. The blue wave has two maxima: one at $+35^\circ$ and another at -10°, with the first maximum to be twice higher than the second. However, the red wave has nearly equal lower amplitudes of the two maxima at the latitudes $\pm 25^\circ$, then another maximum at -55°, and wide flat maximum at 55°. This indicates that the sextuple wave propagation is skewed towards the Northern hemisphere.

For the last pair of latitudinal waves, octuple waves (Fig. 8, bottom right plot), one can observe again the two, positive and negative, waves with four equal amplitude maxima for red wave and four decreasing amplitude maxima for the blue wave. The fluctuations of these two components are in phase, having their maxima at latitudes $+50^\circ$, $+15^\circ$, -20°, and 55° and the minima in between.

The links of some of these latitudinal waves to the temporal ones and to the observational features of solar activity are discussed below in Section 3.

3 LINKS OF THE SUMMARY CURVES TO SOLAR ACTIVITY FEATURES

3.1 Summary curve for dipole PCs and averaged sunspot numbers

Averaged sunspot numbers on the solar disc are considered to be the current solar activity index (Schwabe 1843; Wolf 1850a, b). Most prediction models for solar activity use this index in various attempts to predict its variations for the future solar cycle(s) (see, for example, Pesnell 2008, 2020, and references therein). The lack of strongly positive fits of the predicted solar activity expressed in expected sunspot numbers with the real solar activity measured later in sunspot numbers, after the prediction has been made, indicates some consistent disagreement between the variables defining the solar activity as modelled in dynamo models and those measured (averaged sunspot numbers). The dynamo models operate with poloidal and toroidal magnetic fields, with the first one being the SBMF considered earlier and the second one being related to the magnetic field of sunspots, which is directly linked to the areas covered by sunspots, or averaged sunspot numbers. However, the latter also contains the number of sunspot groups that clearly deviates from the total magnetic field of sunspots.

Since the SBMF is shown to be in antiphase with the leading polarity of magnetic field in sunspots (Stix 1976; Zharkov et al. 2008) defining the locations and timing of sunspot appearances on the solar surface and their migration towards the solar equator or poles (Zharkov et al. 2008), one can expect that the summary curve of the SBMF should reveal its well-defined link with the averaged sunspot numbers. The link of the summary curve of these PCs with the solar activity index of the average sunspot numbers reported by Shepherd et al. (2014) and Zharkova et al. (2015) can be clearly understood because these PCs, in fact, reflect the magnetic butterfly diagrams linked to sunspot occurrences (Cadavid et al. 2005; Lawrence et al. 2005).

Given the fact that these two entities (SBMF and sunspots) define different magnetic field of solar dynamo action (poloidal and toroidal) defined by different differential equations, and the

difference between the solar activity index defining the averaged sunspot numbers from the real toroidal field of the magnetic loops forming sunspots and active regions, one can expect that this link should be more causal than identical. None the less, let us now check how the summary curve can be fitted to the current index of solar activity – averaged sunspot numbers. The annual numbers of sunspot were taken from the Solar Influences Data Analysis Center (SIDC) at the Royal Observatory of Belgium (SILSO World Data Center 2021).

By visually comparing the summary curve with the differences between sunspot numbers in Northern and Southern hemispheres in cycles 21–24 shown in Fig. 4, it becomes evident that the sunspot asymmetry loosely follows the summary curve or the dominant PC defining this curve. For example, in cycle 21 the dominance of the PC2 with southern polarity at the times close to the cycle maximum coincides with the dominance of sunspot numbers in the Southern hemisphere. Shortly later this is changed to a dominance of the PC1 with northern polarity and prevailing numbers of sunspots in the Northern hemisphere. The similar tendencies can be seen for other cycles.

In order to link the variations of the summary curve of SBMF to solar activity index using the properties of sunspot and group index expressed in positive numbers, let us calculate, as suggested by Zharkova et al. (2015), the modulus summary curve (MSC) of the SBMF PCs for cycles 21–24 taken from Fig. 4 by using the absolute values of the negative PC associated with southern polarity of a magnetic field. The overplot of this MSC on to the averaged sunspot numbers (SILSO World Data Center 2021) for solar cycles 21–24 is presented in Fig. 9 (bottom plot).

One can note a remarkable resemblance between these two curves, given the fact that they represent different magnetic components of solar dynamo waves: poloidal for the MSC and toroidal for averaged sunspot numbers. The modulus curve follows, in general, the averaged sunspot numbers for all four cycles as evident from the plot. In the previous comparison of these curves for cycles 21–23, there were some discrepancies between these curves for the descending phase of cycle 23 (Zharkova et al. 2015), which was later explained by the strongly inflated sunspot numbers used at Locarno observatory (Clette et al. 2014; Cliver et al. 2015). Now the corrected averaged sunspot numbers fit much better the MSC in cycle 23 presented in Fig. 9 (bottom plot).

Embracing this similarity between the MSC and averaged sunspot numbers, the MSC can be normalized for each cycle by the averaged sunspot numbers, which is now reflected in the left *Y*-axis of Fig. 9, bottom plot. The modulus curve, in general, follows the averaged sunspot numbers for all the the cycles revealing a significant reduction of solar activity from cycle 21 (maximum about 300 sunspots), through cycle 22 (230), 23 (165), to cycle 24 (108). This fits reasonably to the maximum numbers reported for cycles 21–24 (SILSO World Data Center 2021): 21 – 233, 22 – 213, 23 – 180, and 24 – 116, keeping in mind that the PCs are derived from the solar background (poloidal) magnetic field while sunspot numbers are related but not equal to the solar toroidal magnetic field.

Hence, on the one hand, the MSC is found to be a good proxy of the traditional solar activity index contained in the averaged sunspot numbers (SILSO World Data Center 2021). On the other hand, this summary curve is a derivative from the PCs of SBMF with the clear mathematical functionalities representing the real physical process – poloidal field dynamo waves – generated by the solar dynamo at the same time (Popova et al. 2013; Zharkova et al. 2015). This suggestion is supported by the recent research of the same SBMF data from WSO (Kitiashvili 2020; Obridko et al. 2021).

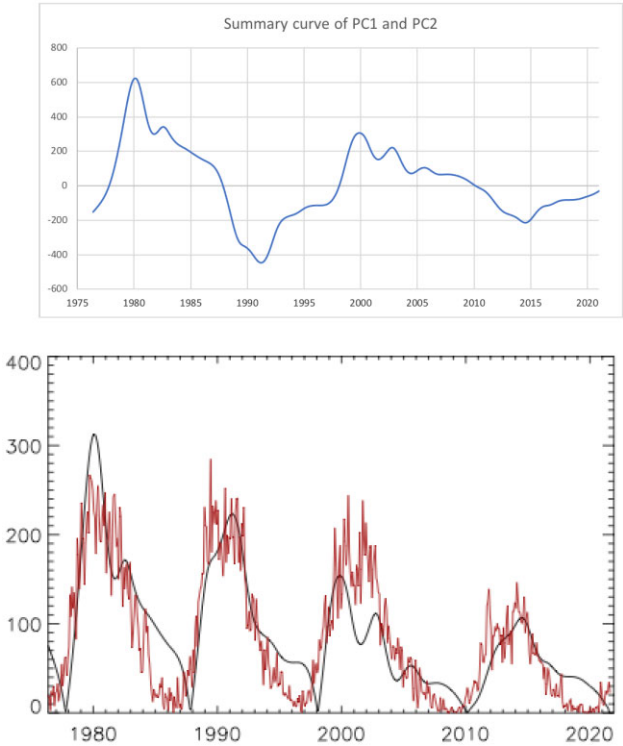

Figure 9. Upper plot: The summary curve (*Y*-axis, arbitrary units) from Fig. 4 calculated from the two PCs versus time (*X*-axis) for cycles 21–24. Bottom plot: The MSCs (arbitrary units) versus time (*X*-axis) derived from the above summary curve overplotted on the averaged sunspot numbers for cycles 21–24. The *Y*-axis shows the averaged sunspot numbers from the Solar Influences Data Analysis Center (SIDC) (SILSO World Data Center 2021).

Therefore, the summary curve of the PCs of SBMF evaluated by averaged sunspot numbers and their north–south asymmetries can be considered as a very reasonable proxy of the traditional solar activity understandable by many observers. The summary curve, in fact, represents the eigenvectors of the poloidal magnetic field of the Sun that can provide a better reproduction of the solar dynamo processes defining solar activity than more artificial index combining sunspot numbers with sunspot groups that hardly can be linked directly to the toroidal magnetic field of the Sun. Plus, the summary curve explicitly adds to this proxy the additional parameter – a dominant polarity of the SBMF for each cycle, which has the polarity opposite to the leading polarity of sunspots (Stix 1976; Zharkov et al. 2008). Also, this summary curve has a mathematical expression, which can be used for medium- and long-term prediction of solar activity useful for many climate studies.

Based on the similarity of the modulus summary and sunspot curves, one can conclude that the solar activity in the cycles 21–24 was systematically decreasing with a cycle number because of the shift in phase of the two magnetic waves so that their phase is increasingly approaching an antiphase when there will be a lack of interaction between these two magnetic waves supposedly produced by solar dynamo. This separation of the two waves into the opposite phases (maximum and minimum) will result in a virtual absence of solar magnetic field on the solar surface, causing, in turn, a lack of magnetic flux tubes appearing on this surface as sunspots. This is likely to lead to a lack of any sunspot activity on the solar surface in cycles 25–27 as predicted by Zharkova et al. (2015), similar to that recorded during the Maunder Minimum in the 17th century (Eddy 1976).

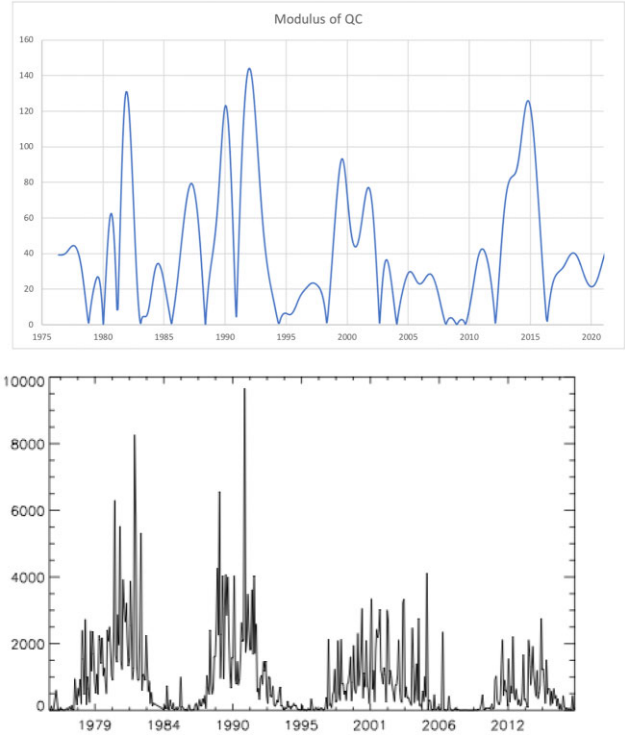

Figure 10. Top plot: The MSC (*Y*-axis, arbitrary units) of QCs of SBMF. Bottom plot: The variations of the SXR emission flux of flares (*Y*-axis, in units of 10^{-6} W m^{-2}) versus time (*X*-axis) for the period 1975–2017 (see the text for details).

3.2 Flare SXR fluxes and quadruple/sextuple magnetic field components

3.2.1 Temporal variations

Let us now explore the role of the QCs and their links to solar activity features and, in particular, the solar activity index in soft X-ray emission flux (FISXR). Previously, Joshi & Joshi (2004) and Joshi et al. (2010, 2015) investigated the existence of intermediate-term periodicities in the X-ray flare index (FISXR), which is based on the continuous record of SXR flares observed by GOES during solar cycles 21 and 22 and part of cycle 23. In this paper, we extended these flare data towards the end of cycle 24, considering the SXR flare data locations and energy flux in the time span of 1976 June 1 to 2017 August 31, which was downloaded from the NOAA site https://www.ngdc.noaa.gov/stp/space-weather/solar-data/solar-features/solar-flares/x-rays/goes/xrs/. To perform the study, we plotted the distribution of the modulus quadruple magnetic field for the period of time of cycles 21–24 shown in Fig. 10, top plot and the time variations of 27-d moving average of the daily SXR fluxes for the period 1976–2004 (Joshi & Joshi 2004) are presented in Fig. 10, bottom plot.

It can be seen that the peaks of the SXR fluxes in solar flares that occurred in cycles 21–24 are very close to the maxima of the MSC obtained from the summary curve for QCs of the SBMF in Fig. 5. We can compare the three peaks named as 1, 2, and 3 appearing between 1980 and 1983 in the observed SXR fluxes of cycle 21 (Fig. 10, bottom plot) with the three maxima in the quadruple modulus curve that occurred between 1980 and 1983 in the quadruple field shown in Fig. 10 (top plot). The next cluster of the observed SXR peaks 4 and 5 is seen at about 1988–89 (4) and 1991–1992 (5), whose timing nicely fits the times of two large maxima 4 and 5 in the same years in the modulus curve for cycle 22. This is followed by the gap between 1994 and 1998 followed by the large maximum 6/7 of the flare SXR flux at about 2000–2001 that coincides with the double maxima 6 and 7 of the quadruple modulus curve. The last maximum 8 is observed in the flare SXR flux in 2015–2016 that corresponds to the wide tall maximum of the quadruple modulus curve between 2013 and 2017. Therefore, the links of the maxima of the quadruple magnetic field components with the maxima of SHR fluxes of solar flares can indicate a very important role of these QCs in the generation of the local flaring activity.

Furthermore, a significant peak of about 3.1–3.2 yr was found in the power spectrum performed with the values of flare numbers in the cycles 21–22 (Vizoso & Ballester 1989). Also, the sunspot areas and H α flare occurrences in cycle 23 have also shown a periodicity of about 2.75 yr (Zharkov et al. 2008; Zharkov & Zharkova 2011). To evaluate whether this peak is linked to the maxima of the quadruple modulus curve, let us count the quadruple wave peaks in the cycles: 21 – 4, 22 – 3, 23 – 4, 24 – 3. Given the averaged cycle duration of 11 yr, one can find that the maxima in cycles 21 and 23 occurred every 2.75 yr, in cycles 22 and 24 – 3.6 yr. The mean of these periods in cycles 21–24 is equal to 3.05 yr that is close the flare peak periods in the flare power spectrum reported by Vizoso & Ballester (1989) for cycles 21–22 and is very close to the period of quadruple field variations found in H α flare and sunspot occurrences in cycle 23 (Zharkov & Zharkova 2011).

These similarities in the maxima locations, amplitudes, and frequencies between the observed SXR fluxes and quadruple modulus curve indicate that the QC of the solar magnetic field plays a very important role in initiating the local solar activity in active regions and flares. The quadruple and sextuple magnetic sources can appear because of the shifts of the magnetic sources in the Northern and Southern hemispheres caused by the differential rotation velocities in the Northern and Southern hemispheres as measured from the observations (Antonucci et al. 1990; Veronig et al. 2001; Temmer et al. 2002). In fact, by predicting the summary and MSCs of QC of the eigenvectors, one can significantly improve the prediction of solar flares and associated events, like coronal mass ejections.

3.2.2 Latitudinal variations versus north–south asymmetries

The latitudinal variations of the PCs, or dipole magnetic waves, are rather symmetric in each hemisphere, which cannot be said about the other waves generated by different magnetic sources. We show that the quadruple magnetic field (see Fig. 8) reveals larger amplitudes in the Southern hemisphere, while the sextuple waves have larger amplitudes in the Northern hemisphere. This can be compared to the observational asymmetries, indicating that, in addition to the magnetic waves produced by dipole sources, there is domination of sextuple magnetic waves in odd cycles and quadruple waves in even cycles. The joint effects of quadruple and sextuple waves can be detected in the observed N–S asymmetries of the flare index in SXR fluxes.

Following a close link of the quadruple magnetic field to the flaring index in SXR fluxes established in Section 3.2, let us now explore the latitudinal variations of magnetic field components, in order to understand the north–south asymmetry often reported in the occurrences of solar flares (Özgüç & Altaş 1996; Joshi & Joshi 2004; Joshi et al. 2010; Zharkov & Zharkova 2011) and sunspots (Temmer et al. 2001; Zharkov et al. 2005). Taking all this into account, here we have made an attempt to investigate the N–S asymmetry of soft

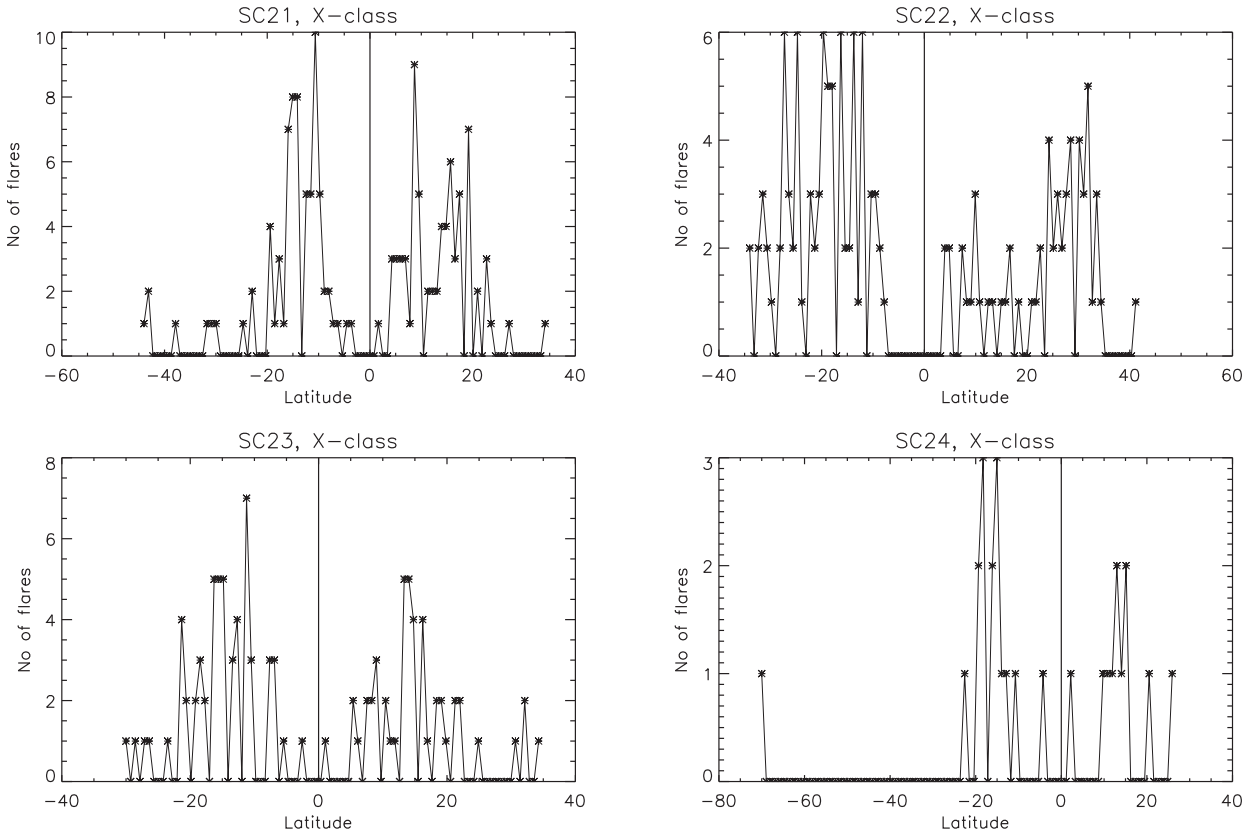

Figure 11. The north–south asymmetry of occurrences of X-class flares in cycles 21 (top left), 22 (top right), 23 (bottom left), and 24 (bottom right).

X-ray flare index (FISXR) presented by Joshi & Joshi (2004) and Joshi et al. (2010), which is based on the continuous record of SXR flares observed by GOES during solar cycles 21, 22, 23, and 24.

The latitudinal distributions of SXR fluxes from flares of different classes in different solar cycles are presented in Figs 11–13 and for the whole number of flares for all four cycles are plotted in Fig. 14. The sign 0° represents the equator of the Sun. The variations of N–S asymmetry for the total SXR fluxes of flares and for the flares of C, M, and X classes reveal the pronounced peaks occurring at 11–20° latitude band on both sides of the solar equator. However, there are consistently higher SXR fluxes in the flares occurring in Southern hemisphere for all classes for cycles 21, 22, and 24. Only in cycle 23 for the flares of classes M and C, the SXR fluxes in both hemispheres have nearly equal numbers.

This latitudinal distribution of number of SXR flares can be interpreted by the latitudinal distributions of PCs, specifically, of the quadruple and sextuple magnetic field components (see Fig. 8 top right and bottom left plots in Section 2.3.4) revealing the dominance of quadruple waves in the Southern hemisphere and sextuple waves in Northern hemisphere (see Fig. 8, bottom left plot). The latitudinal variations of the PCs, or dipole magnetic waves, are rather symmetric in each hemisphere, which cannot be said about the other waves generated by different magnetic sources. We show that the quadruple magnetic field (see Fig. 8) reveals larger amplitudes in the Southern hemisphere, while the sextuple waves have larger amplitudes in the Northern hemisphere. The latitudinal distributions of SXR fluxes from flares of different classes in different solar cycles presented in Figs 11–13 and 14 with evident dominance of Southern hemisphere in the production of flares with highest SXR fluxes confirm the leading role of quadruple magnetic waves in a formation of flares, since quadruple waves have a dominance in Southern hemisphere.

The close magnitudes in latitudinal distributions of SXR flares with highest fluxes for C-class flares, evidently, indicate that in upper atmospheric layers where X- and M-class flares occur, the quadruple magnetic components prevail, while in lower atmospheric layers where C-class flares and sunspots occur, SCs become dominant. This finding lends the support to the different shifts of magnetic sources in the Northern and Southern hemispheres caused by the differential rotation velocities as measured from the observations (Antonucci et al. 1990; Veronig et al. 2001; Temmer et al. 2002).

Furthermore, temporal variations of the N–S asymmetry indices for the total number of SXR flares with different intensity classes (B, C, M, and X) based on the annual SXR flux counts from 1976 to 2007 [see Fig. 15, bottom plot (Joshi et al. 2010)] also reveal the oscillations in latitudes with a dominance of Northern hemisphere in odd and Southern hemisphere in even cycles. These variations can be compared with the variations of the quadruple and sextuple summary curves presented in Fig. 15, top and middle plots, respectively.

It can be seen from the observational N–S asymmetry of flare occurrences (Fig. 15, bottom plot) that initially during cycle 21, the Northern hemisphere was more active but after 1980 it was shifted slightly towards south. In fact, in the year 1983 the activity moved strongly towards Southern hemisphere and prevailed there during most of the cycle 22 following the propagation of two PCs shown in Fig. 4. In the cycle 23, there is a strong peak in Southern hemisphere during the minimum phase in the year 1996 and then the activity is moved towards the north. In the years 1998, 1999, and 2000, the flare occurrence in the Northern hemisphere dominated. Then, after

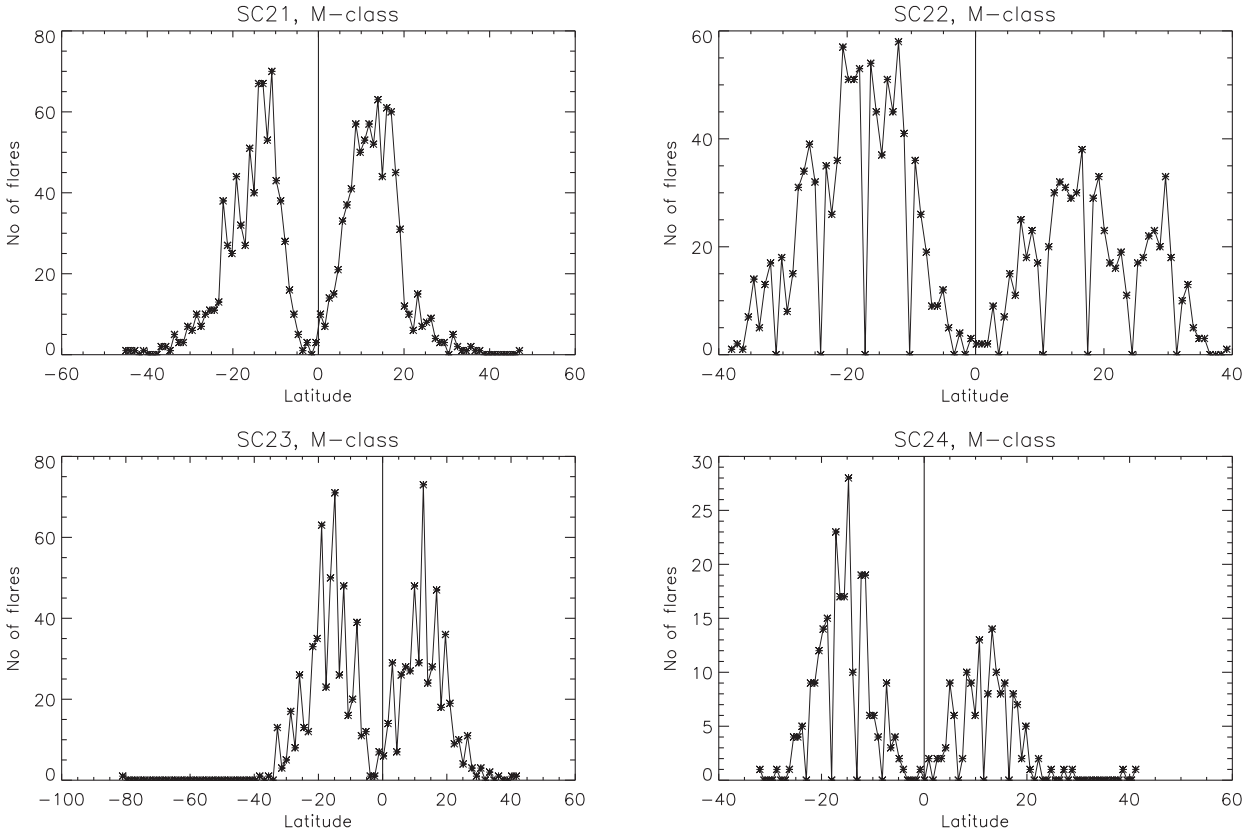

Figure 12. The north–south asymmetry of occurrences of M-class flares in cycles 21 (top left), 22 (top right), 23 (bottom left), and 24 (bottom right).

2000 there started a clear domination of the Southern hemisphere with a sharp peak in 2006. These results are in agreement with the work done by Temmer et al. (2001) and Veronig et al. (2001), who analysed the N–S asymmetry of H α flares from 1975 to 1999, or the N–S asymmetry in H α flares in cycle 23 (Zharkov & Zharkova 2011). The preference for Northern hemisphere during the rising phase of cycle 23 is also reported by Ataç & Özgüç (2001) with the data of H α flares.

By comparing the quadruple and sextuple curves with the observations of the N–S asymmetries of SXR fluxes of solar flares shown in Fig. 15, one can observe the close visual resemblance of the summary curve of the sextuple magnetic field (Fig. 15, middle plot) to the observed curve of the N–S asymmetries plotted in Fig. 15, bottom plot. Combining the plots for the temporal and latitudinal distributions of quadruple and sextuple components of magnetic field waves of SBMF, it is possible to deduce how these waves propagate over the solar latitudes for each cycle and to deduce that the quadruple summary curve dominates the intensity of SXR fluxes in all cycles. However, the interaction between quadruple and sextuple waves can define a number of flares occurring in different cycles. Keep in mind that the quadruple waves in the even cycles 22 and 24 are much stronger than those in cycles 21 and 23 (see Fig. 15, top plot) and because of it, the effect of sextuple waves becomes noticeable in the odd cycles. As a result, the flare occurrence distributions fluctuate over latitudes becoming skewed towards the southern latitudes in even cycles and northern ones in odd ones.

Hence, the dominance of SXR flares with largest fluxes produced in Southern hemisphere and the oscillating numbers of flares produced in Northern and Southern hemispheres in the odd and even cycles indicate that the magnetic waves from quadruple and sextuple magnetic sources should play the key role in the initiation of a flaring activity and associated eruptions. The summary curves of quadruple and sextuple magnetic waves generated at different depths by variable differential rotation of the opposite hemispheres can be strong additional factors resulting in more reliable prediction of solar flare occurrences and their maximal SXR fluxes.

4 DISCUSSION AND CONCLUSIONS

4.1 Discussion

In this paper, we updated PCA of the synoptic maps of the SBMF obtained by WSO to four cycles 21–24 and derived the first eight eigenvectors covering the majority of the magnetic data by variance. We confirm our previous findings of the eigenvalues and eigenvectors derived from the data obtained for cycles 21-23 and reveal that the eigenvalues remain the same for the extended data including cycle 24. The eigenvectors of the SBMF are found to appear in pairs, with the total four pairs covering more than 88 per cent of the total data variance.

The two PCs newly derived here for cycles 21–24 are compared with those obtained earlier for cycles 21–23 (Zharkova et al. 2012, 2015). The results of this comparison clearly reveal that both the PC curves for cycles 21–24 and 21–23 have a nearly identical fit, following the same directions and functionalities that confirm the previous results derived from the data for cycles 21–23 (Shepherd et al. 2014; Zharkova et al. 2015). The summary curve of the two PCs covering 39 per cent of data by variance, assigned to the magnetic waves generated by dipole magnetic sources, shows a steady decrease

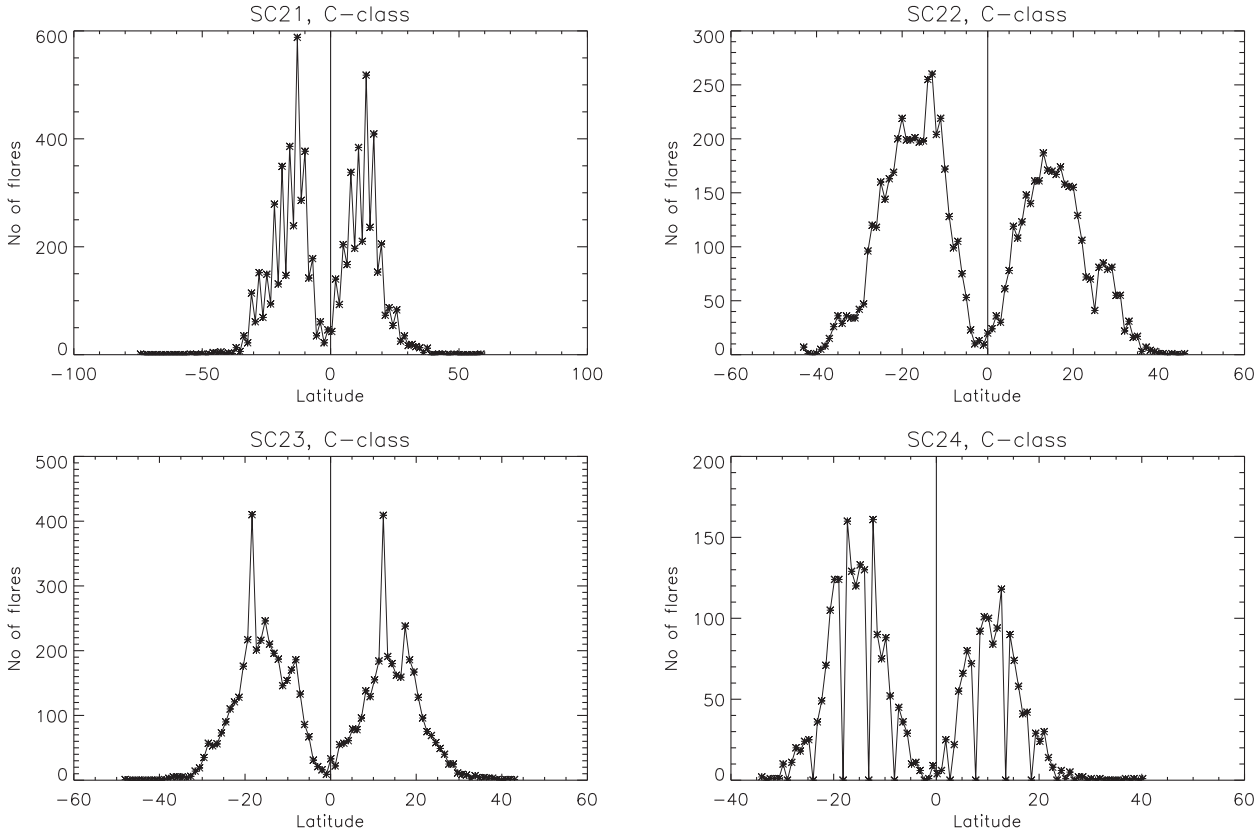

Figure 13. The north–south asymmetry of occurrences of C-class flares in cycles 21 (top left), 22 (top right), 23 (bottom left), and 24 (bottom right).

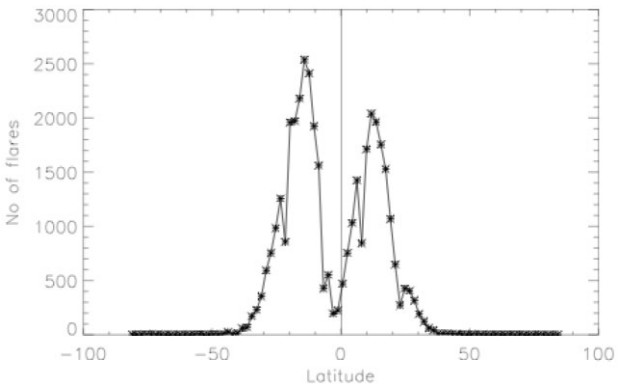

Figure 14. The north–south asymmetry of occurrences of flares of all classes in the period 1975–2017 (cycles 21–24).

of the amplitudes from cycles 21 to 24. The decay of the wave amplitudes for both PC waves is intrinsic to the mechanisms of solar dynamo acting in two layers of solar interior responsible for generating the two main waves for the poloidal magnetic field detected as two PCs of SBMF.

The previous PCA and ICA carried out by Lawrence et al. (2005) and Cadavid et al. (2005, 2008) using the NSO higher resolution magnetic synoptic maps did not reveal clear pairs of the PCs found by Zharkova et al. (2012). This is believed to happen due to much higher spatial resolution of the NSO full disc magnetic data, which includes not only the solar background (poloidal) magnetic field but also the (toroidal) magnetic fields of active regions clearly shown in the magnetic 'butterfly diagrams' (Cadavid et al. 2005; Lawrence et al. 2005). This means that the NSO data entered into the PCA by Lawrence et al. (2005) and Cadavid et al. (2005, 2008) were strongly contaminated by the magnetic field of active regions and sunspots (reaching up to 1000 G). However, the WSO low-resolution magnetic data have these active region magnetic fields significantly smoothed to match the background field. Each set of PCs (Lawrence et al. 2005; Zharkova et al. 2012) has its own value for the dynamo modelling while both the data become rather close at higher latitudes, emphasizing a role of SBMF via the polar magnetic field (Benevolenskaya 1996, 1998; Cadavid et al. 2005; Choudhuri et al. 2007; Zharkova et al. 2015).

We also added the further three pairs of the PCs, the waves allegedly generated by quadruple, sextuple, and octuple magnetic sources, describing their temporal and latitudinal properties. The two eigenvectors of the quadruple (principal) components (QCs) are derived with PCA from the SBMF covering the other 16.6 per cent of the whole solar magnetic field data by variance. The temporal variations of quadruple and sextuple components are essentially different from those of two PCs produced by dipole sources. QC amplitudes are found nearly twice smaller than those of the PCs, the sextuple amplitudes are nearly 30 per cent smaller than quadruple one, and the octuple amplitudes again are 50 per cent smaller than the sextuple ones. The latitudinal variations of the dipole waves are rather symmetric in both hemispheres, while the QCs are skewed towards Southern hemisphere and sextuple waves are skewed more towards Northern hemisphere. The octuple reveals again nearly symmetric wave distributions with a few maxima appearing in each hemisphere.

On the one hand, since the SBMF is in antiphase with the leading polarity of magnetic field in sunspots (Stix 1976) SBMF defines the

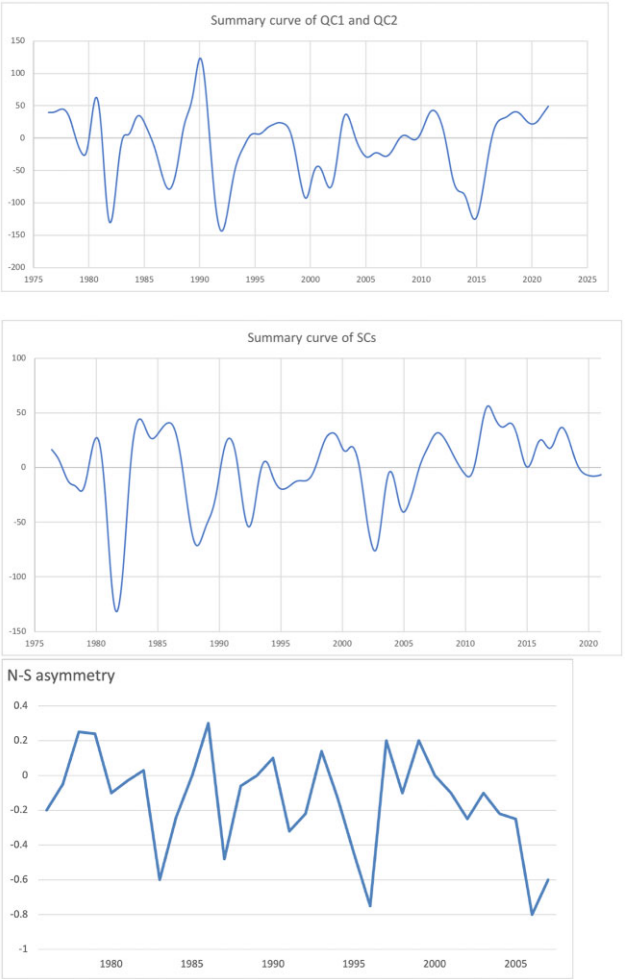

Figure 15. Top: the summary curve (*Y*-axis, arbitrary units) of QCs of SBMF with their polarities (positive for northern and negative for southern) versus time (*X*-axis). Middle: the summary curve (*Y*-axis, arbitrary units) of SCs of SBMF versus time (*X*-axis). Bottom: the north–south asymmetry of monthly SXR flares (*Y*-axis) for the period 1975–2008 (cycles 21–24), similar to the solid curve in fig. 4 by Joshi et al. (2010).

locations and timing of sunspot appearances on the solar surface (Zharkov et al. 2008), which, in turn, can explain why the summary curve of the SBMF should have a well-defined link with the averaged sunspot numbers. The MSC of two PCs from dipole sources for cycles 21–24 was overplotted on to the averaged sunspot numbers reveals a remarkable resemblance despite the fact that they represent different magnetic components of solar dynamo waves: poloidal for the MSC and toroidal for averaged sunspot numbers. The modulus curve follows, in general, the averaged sunspot numbers for all four cycles, revealing a significant reduction of solar activity from cycle 21 (maximum 300 sunspots), through cycle 22 (230), 23 (165), to cycle 24 (108).

On the other hand, maxima of the MSC obtained from the summary curve for QCs of the SBMF are very close to the peaks of the SXR fluxes in solar flares that occurred in cycles 21–24, which can indicate a very important role of the QCs in the generation of the local solar activity in active regions. Interestingly, there are regular peaks, or multiple maxima of the quadruple modulus curve, occurring with a period varying between 2.75 yr for odd cycles and 3.6 yr for even ones, or an averaged period of 3.05 yr, which is close to the periods of 2.75–3.2 yr derived from the observational periodicity of flaring activity (Vizoso & Ballester 1989; Zharkov & Zharkova 2011).

The joint effects of quadruple and sextuple waves can be detected in the observed N–S asymmetries of the SXR flare numbers. The dominance of SXR flares with largest fluxes produced in Southern hemisphere and oscillating numbers of flares produced in Northern and Southern hemispheres in the odd and even cycles indicate that the magnetic waves from quadruple and sextuple magnetic sources should play the key role in the initiation of a flaring activity and associated eruptions. These waves can be strong additional factors leading to more reliable prediction of solar flare occurrences and maximal SXR fluxes.

4.2 Summary

In summary, in this paper we managed to:

(i) Confirm with the data for cycles 21–24 the eigenvalues and eigenvectors of SBMF derived from cycles 21 to 23.

(ii) Explain a difference between the PCA results derived from the low-resolution WSO and high-resolution NSO magnetic maps.

(iii) Confirm a summary curve of two PCs as a new additional proxy of solar activity close to sunspot solar index.

(iv) Introduce a link of the quadruple pair of PCs to the flare SXR flux index.

(v) Show that the additional three pairs of PCs are linked to biennial (2–3 yr) periodicity of flare occurrences for different classes of flares.

(vi) Link latitudinal variations of different PCs to the north–south asymmetries observed in sunspots and flare occurrences.

Further investigation is required for the magnetic field components derived with PCA to confirm the prediction of solar activity (Shepherd et al. 2014; Zharkova et al. 2015), to refine the timing of the GSMs in the past and the future and to confirm the role of double solar dynamo in generation of these waves, which will be a scope of the forthcoming paper.

ACKNOWLEDGEMENTS

The authors would like to thank the Solar Influences Data Analysis Center (SIDC) at the Royal Observatory of Belgium for providing the corrected averaged sunspot numbers and to the National Oceanic and Atmospheric Administration (NOAA) for providing the flare data. The authors also express their deepest gratitude to the staff and directorate of WSO for providing the coherent long-term observations of full disc synoptic maps of the SBMF. Also, the authors would like to thank very much the valuable help of Dr. S. Zharkov (Hull University, UK) for finding the data and producing the bulk of important plots related to the observational aspects of sunspots and flares that helped enormously to carry out the analysis.SMBF - solar background magnetic field, UK - United Kingdom. The authors acknowledge the funding of this research by the ZVS Research Enterprise Ltd.

DATA AVAILABILITY

The data underlying this article will be shared on reasonable request to the corresponding author.

REFERENCES

Antonucci E., Hoeksema J. T., Scherrer P. H., 1990, ApJ, 360, 296
Atac T., 1989, Earth Moon Planets, 47, 165

Ataç T., Özgüç A., 1996, Sol. Phys., 166, 201
Ataç T., Özgüç A., 2001, Sol. Phys., 198, 399
Benevolenskaya E. E., 1995, Sol. Phys., 161, 1
Benevolenskaya E. E., 1996, Sol. Phys., 167, 47
Benevolenskaya E. E., 1998, ApJ, 509, L49
Cadavid A. C., Lawrence J. K., McDonald D. P., Ruzmaikin A., 2005, Sol. Phys., 226, 359
Cadavid A. C., Lawrence J. K., Ruzmaikin A., 2008, Sol. Phys., 248, 247
Carbonell M., Oliver R., Ballester J. L., 1993, A&A, 274, 497
Chatzistergos T., Usoskin I. G., Kovaltsov G. A., Krivova N. A., Solanki S. K., 2017, A&A, 602, A69
Choudhuri A. R., Chatterjee P., Jiang J., 2007, Phys. Res. Lett., 98, 131103
Clette F., Svalgaard L., Vaquero J. M., Cliver E. W., 2014, Space Sci. Rev., 186, 35
Cliver E. W., Clette F., Svalgaard L., Vaquero J. M., 2015, Cent. Eur. Astrophys. Bull., 39, 1
Eddy J. A., 1976, Science, 192, 1189
Golub G. N., Kahhan W., 1965, J. Soc. Ind. Appl. Math. Ser. B: Numer. Anal., 2, 205
Golub G., Van Loan C., 1996, Matrix Computations. Johns Hopkins Univ. Press, Baltimore, MD
Hathaway D. H., 2015, Living Rev. Sol. Phys., 12, 4
Hathaway D. H., Wilson R. M., Reichmann E. J., 2002, Sol. Phys., 211, 357
Hoeksema J. T., 1984, PhD thesis, AA. Stanford Univ., Stanford, CA
Jolliffe I. T., 2002, Principal Component Analysis, 2nd edn. Springer Ser. Stat., Berlin
Joshi A., 1999, Sol. Phys., 185, 397
Joshi B., Joshi A., 2004, Sol. Phys., 219, 343
Joshi N. C., Bankoti N. S., Pande S., Pande B., Uddin W., Pandey K., 2010, New Astron. J., 15, 538
Joshi B., Bhattacharyya R., Pandey K. K., Kushwaha U., Moon Y.-J., 2015, A&A, 582, A4
Kitiashvili I. N., 2020, ApJ, 890, 36
Lawrence J. K., Cadavid A., Ruzmaikin A., 2005, Sol. Phys., 225, 1
Leussu R., Usoskin I. G., Arlt R., Mursula K., 2016, A&A, 592, A160
Lockwood M., Owens M. J., Barnard L., Davis C. J., Steinhilber F., 2011, Geophys. Res. Lett., 38, 22105
McComas D. J. et al., 2018, Space Sci. Rev., 214, 116
Obridko V. N., Sokoloff D. D., Pipin V. V., Shibalvaa A. S., Livshits I. M., 2021, J. Atmos. Sol.-Terr. Phys., 225, 105743
Oliver R., Ballester J. L., 1994, Sol. Phys., 152, 481
Özgüç A., Altaş L., 1996, Sol. Phys., 163, 327
Özgüç A., Ataç T., Rybák J., 2003, Sol. Phys., 214, 375
Pap J. M., Willson R. C., Donnelly R. F., 1992, in Harvey K. L., ed., ASP Conf. Ser. Vol. 27, The Solar Cycle. Astron. Soc. Pac., San Francisco, p. 491
Pesnell W. D., 2008, Sol. Phys., 252, 209
Pesnell W. D., 2020, J. Space Weather Space Clim., 10, 60
Popova E., Zharkova V., Zharkov S., 2013, Ann. Geophys., 31, 2023
Popova E., Zharkova V., Shepherd S., Zharkov S., 2018, J. Atmos. Sol.-Terr. Phys., 176, 61
Ravindra B., Chowdhury P., Javaraiah J., 2021, Sol. Phys., 296, 2
Schmidt M., Lipson H., 2009, Science, 324, 81
Schwabe M., 1843, Astron. Nachr., 20, 283
Shepherd S. J., Zharkov S. I., Zharkova V. V., 2014, ApJ, 795, 46
SILSO World Data Center, 2021, International Sunspot Number Monthly Bulletin and Online Catalogue, Available at https://wwwbis.sidc.be/silso/datafiles
Solanki S. K., Krivova N. A., 2011, Science, 334, 916
Solanki S. K., Usoskin I. G., Kromer B., Schüssler M., Beer J., 2004, Nature, 431, 1084
Stix M., 1976, A&A, 47, 243
Svalgaard L., Schatten K. H., 2016, Sol. Phys., 291, 2653
Temmer M., 2021, Living Rev. Sol. Phys., 18, 4
Temmer M., Veronig A., Hanslmeier A., Otruba W., Messerotti M., 2001, A&A, 375, 1049
Temmer M., Veronig A., Hanslmeier A., 2002, A&A, 390, 707
Usoskin I. G., 2008, Living Rev. Sol. Phys., 5, 3
Usoskin I. G., 2017, Living Rev. Sol. Phys., 14, 3
Usoskin I. G., 2018, J. Atmos. Sol.-Terr. Phys., 176, 69
Usoskin I., Kovaltsov G., 2015, preprint (arXiv:e-print)
Usoskin I., Solanki S., Moss D., 2009, Solar Physics, 254, 345
Velasco Herrera V. M., Soon W., Legates D. R., 2021, Adv. Space Res., 68, 1485
Veronig A., Vršnak B., Temmer M., Magdalenić J., Hanslmeier A., 2001, Hvar Obs. Bull., 25, 39
Veronig A. M., Jain S., Podladchikova T., Pötzi W., Clette F., 2021, A&A, 652, A56
Vizoso G., Ballester J. L., 1989, Sol. Phys., 119, 411
Wolf R., 1850a, Astron. Mitt. Eidgenössischen Sternwarte Zürich, 1, 3
Wolf R., 1850b, Astron. Mitt. Eidgenössischen Sternwarte Zürich, 1, 15
Zharkov S. I., Zharkova V. V., 2006, Adv. Space Res., 38, 868
Zharkov S. I., Zharkova V. V., 2011, J. Atmos. Sol.-Terr. Phys., 73, 264
Zharkov S., Zharkova V. V., Ipson S. S., 2005, Sol. Phys., 228, 377
Zharkov S., Gavryuseva E., Zharkova V., 2008, Sol. Phys., 248, 339
Zharkova V., 2020, Temperature, 7, 217
Zharkova V. V., Shepherd S. J., Zharkov S. I., 2012, MNRAS, 424, 2943
Zharkova V. V., Shepherd S. J., Popova E., Zharkov S. I., 2015, Nat. Sci. Rep., 5, 15689
Zharkova V. V., Shepherd S. J., Popova E., Zharkov S. I., 2017, preprint (arXiv:1705.04482)
Zharkova V., Popova E., Shepherd S., Zharkov S., 2018, J. Atmos. Sol.-Terr. Phys., 176, 72

This paper has been typeset from a TEX/LATEX file prepared by the author.